Dynamic simulation of Adiabatic Compressed Air Energy Storage (A-CAES) plant with integrated thermal storage – Link between components performance and plant performance

Sciacovelli, Adriano; Li, Yongliang; Chen, Haisheng; Wu, Yuting; Wang, Jihong; Garvey, Seamus; Ding, Yulong

DOI:
10.1016/j.apenergy.2016.10.058

Document Version
Peer reviewed version

Citation for published version (Harvard):
Sciacovelli, A, Li, Y, Chen, H, Wu, Y, Wang, J, Garvey, S & Ding, Y 2017, 'Dynamic simulation of Adiabatic Compressed Air Energy Storage (A-CAES) plant with integrated thermal storage – Link between components performance and plant performance', *Applied Energy*, vol. 185, no. Part 1, pp. 16-28.
https://doi.org/10.1016/j.apenergy.2016.10.058

Dynamic simulation of Adiabatic Compressed Air Energy Storage (A-CAES) plant with integrated thermal storage – link between components performance and plant performance

Adriano Sciacovelli[*a], Yongliang Li[a], Haisheng Chen[b], Yuting Wu[c], Jihong Wang[d], Seamus Garvey[e], Yulong Ding[a]

[a]Birmingham Centre for Energy Storage, School of Chemical Engineering, University of Birmingham, Birmingham, B15 2TT, UK
[b]Institute of Engineering Thermophysics, Chinese Academy of Sciences, Beijing, 100190, China
[c]Key Laboratory of Enhanced Heat Transfer and Energy Conservation, Beijing University of Technology, Beijing, China
[d]School of Engineering, University of Warwick, UK
[e]Faculty of Mechanical Engineering, University of Nottingham, Nottingham NG7 2RD, United Kingdom
* Corresponding author. Email: a.sciacovelli@bham.ac.uk; Tel. +44 (0)121 415 8866;

Abstract

The transition from fossil fuels to green renewable resources presents a key challenge: most renewables are intermittent and unpredictable in their nature. Energy storage has the potential to meet this challenge and enables large scale implementation of renewables. In this paper we investigated the dynamic performance of a specific Adiabatic Compressed Air Energy Storage (A-CAES) plant with packed bed thermal energy storage (TES). We developed for the first time a plant model that blends together algebraic and differential sub-models detailing the transient features of the thermal storage, the cavern, and the compression/expansion stages. The model allows us to link the performance of the components, in particular those of the thermal storage system, with the performance of the whole A-CAES plant. Our results indicate that an A-CAES efficiency in the range 60-70% is achievable when the TES system operates with a storage efficiency above 90%. Moreover, we show how the TES dynamic behaviour induces off-design conditions in the other components of the A-CAES plant. Such device-to-plant link of performance is crucial: only through integration of TES model in the whole A-CAES model is possible to assess the benefits and added value of thermal energy storage. To the authors' knowledge the present study is the first of this kind for an A-CAES plant.

Nomenclature

A	Area (m^2)
C	Heat capacity rate ($J\ s^{-1}\ K^{-1}$)
D,d	Diameter (m)
c_p	Specific heat ($J\ kg^{-1}\ K^{-1}$)
Ex_{in}	Exergy flux ($W\ K^{-1}$)
$\dot{G}$	Reduced flow rate (-)
h	Specific enthalpy ($J\ kg^{-1}$)
h_v	Volumetric heat transfer coefficient ($W\ m^{-3}\ K^{-1}$)
H	Height (m)
k	Specific heat ratio (-)
k_a, k_s	Thermal conductivity ($W\ m^{-1}\ K^{-1}$)
$\dot{m}$	Mass flow rate ($kg\ s^{-1}$)
m	Mass (kg)
$\dot{n}$	Reduced speed (-)
p	Pressure (Pa)
T	Temperature (K)
U	Overall heat transfer coefficient ($W\ m^{-2}\ K^{-1}$)
u	Velocity ($m\ s^{-1}$)
W	Power (W)

Greek letters

α	Influence factor (-)
β	Compression ratio (-)
ε	Effectiveness, void fraction (-)
η	Isoentropic efficiency (-)

η_{cycle}	Round trip efficiency (-)
η_{th}	Thermal storage efficiency (-)
π	Expansion ratio (-)
ρ	Density (kg m^{-3})
Φ	Heat transfer rate (W)

1 Introduction

In 2013 the electricity production has reached 23 000 TWh/year of which oil, natural gas, and other fossil fuels account for 68% while renewable sources contribute for less than 6% [1]. Overcome this energy scenario is imperative as CO_2 emissions and global warming are already taking their toll on our society and planet Earth [2]. To contain global warming below 2°C carbon dioxide emission must decrease by 90% by 2050 through an intense penetration of renewable resources which could reach a global share of 65% according to scenarios forecasted by IEA [3]. This great potential can be untapped only if the intrinsic variability of renewables, such wind and solar energy, is mitigated through energy storage (ES). ES technology provides several functions to facilitate the use of renewables: it enables to capture "wrong time" energy and make it available when needed, it helps to shave and shift load peaks, and it improves reliability of energy systems [4,5].

Alongside with pumped hydroelectricity storage, compressed air energy storage (CAES) is among the few grid-scale energy storage technology with power rating of 100s MW [6,7]. CAES operates in such a way that electrical energy is stored in the form of compressed air confined in a natural or artificial reservoir. Then, during periods of high energy demand, stored energy is retrieved by withdrawing high pressure air and expand it through a series of turbines to generate electricity. Traditionally, for example in the Huntorf plant [7,8], before expansion air is heated in a combustion chamber burning conventional fossil fuels. This leads to two drawbacks: CAES is not CO2 free and round trip efficiency is limited to 40-50% [6,7]. To overcome such disadvantages adiabatic compressed air energy storage (A-CAES) has been proposed. Instead of burning fuel, in A-CAES the heat generated by compression is stored in a Thermal Energy Storage (TES) and then used to heat air from the reservoir before it enters the turbines [7,9]. As a result, round trip efficiency increases to 70-75% according to [7,10,11] and fuel consumption is avoided. The vast majority of the studies on A-CAES consider indirect heat exchangers (HEXs) and a separate thermo-fluid to store the heat of compression [9,11-18]. The heat of compression, exchanged via air-to-fluid HEXs, increases the internal energy of the working fluid which acts as a sensible heat storage medium. Commonly, HEXs have been considered installed between each compression stage, to store heat, and between each expansion stage to retrieve heat during discharge fo ACAES plant [11-18].

Another proposed A-CAES configuration uses a solid medium, typically natural rocks, to store the heat of compression [7,19]: during A-CAES charging heat is stored by flowing hot air from compressors through a packed bed of rocks; when discharge occurs air from the cavern flows through the packed bed retrieving the heat previously stored and then expands through turbines train to generate electricity. Literature presents multiple studies on packed beds dealing with the design [20-24], the heat transfer performance [25-30], and the effect of operating conditions [31-34]. However, the *dynamic performance* of A-CAES plant with an integrated packed bed thermal storage remain unaddressed. With this study we fill such a gap in the literature by presenting for the first time a full investigation of an A-CAES plant with packed bed thermal storage. The mathematical model we developed is fully dynamic and it includes off-design performance of each component of the A-CAES plant. The model blends together algebraic and differential sub-models that detail the transient features of the thermal storage, the cavern, and the compression/expansion stages. This allows to link the performance of the components, in particular those of the thermal storage system, with the performance of the

whole A-CAES plant. Such device-to-plant link is crucial: only through integration of TES in the whole A-CAES system is possible to assess the benefit and added value of thermal energy storage. To the authors' knowledge the present study is the first of this kind for an A-CAES plant.

2 System description

Figure 1 presents the specific adiabatic compressed air energy storage system (A-CAES) studied in this work. Table 1 summarizes the major features of the A-CAES plant. A packed bed thermal energy storage (TES) ensures the "adiabatic" conditions: after the HPC compression stage, hot air flows through the packed bed and exchanges heat with the gravel contained in the TES. The gravel acts as sensible storage material and captures heat for later purposes. Air leaves the TES system nearly at ambient temperature and enters the cavern at high pressure. It is worth noting that we focused on a specific A-CAES configuration. A Similar plant configuration is also considered by RWE Power in the EU project "ADELE" [35] and by Airlight Energy [36] although other A-CAES designs are also possible [6,11,14,17,18].

An inter-refrigeration heat exchanger cools the air flow before it enters the high pressure stage. This configuration was also considered in [7] to prevent excessively high air temperature at the outlet of HPC. The compressors operate over a range of compression ratios since air pressure in the caver spans the range 46 to 72 bar, which is the typical range adopted for the Huntorf plant and Machintosh plant [7,8]. The cavern's size considered is a typical one for natural salt caverns [6,7]. During the discharge process, energy is retrieved by withdrawing air from the cavern at high pressure and expand it through the train of turbines. Two discharge modes have been considered in the literature: variable inlet pressure and constant inlet pressure [7,37]. In the former one high pressure air from the cavern directly expands through the turbines which therefore experience a variable (in time) expansion ratio. We considered constant inlet pressure mode: as depicted in Fig. 1, a throttling system maintains the turbine inlet pressure constant. Such an operating mode allows to operate the turbine train at constant expansion ratio and near to design conditions – thus at maximum efficiency – for the entire discharge process. Design expansion ratio (Table 1) for HPT and LPT were chosen as the one for existing CAES plants [8]. Tables 2 and 3 present the thermodynamic state points for compression and expansion under design conditions. The thermodynamic properties were evaluated with EES (Engineering equation solver) using the data in Table 1 as input parameter. For the design conditions reported in Tables 2 and 3 we considered the same temperature for the air temperature at compressor outlet (point 1) and the air temperature at the outlet of TES (point 4). Clearly, a temperature drop is expected under operation (that is $T_1 > T_4$) because of finite heat transfer between air and the filling material of the TES. As illustrated in the Results section T_1 and T_4 differs minimally which support the assumption, for design calculations, of $T_1 = T_4$.

For the purpose of simulation of A-CAES plant operation we considered *n* equal cycles of 10 hours charge, 4 hours discharge and 10 hours idle, as shown in Figure 2. Such a figure present the nominal cycle with constant power input during charge and constant power output during discharge. The actual profile of each cycle was determined through the simulations performed, as detailed in the Results section. The nominal profile of Fig. 2 was chosen considering the A-CAES plant operating for peak shaving, minute reserve, or compensation of fluctuation in wind power. Such operation modes are typical of existing CAES plants [7,8], and present discharge time of 3-4 hours, as in the case of Fig. 2. The total number *n* of cycles considered in the study was 30.

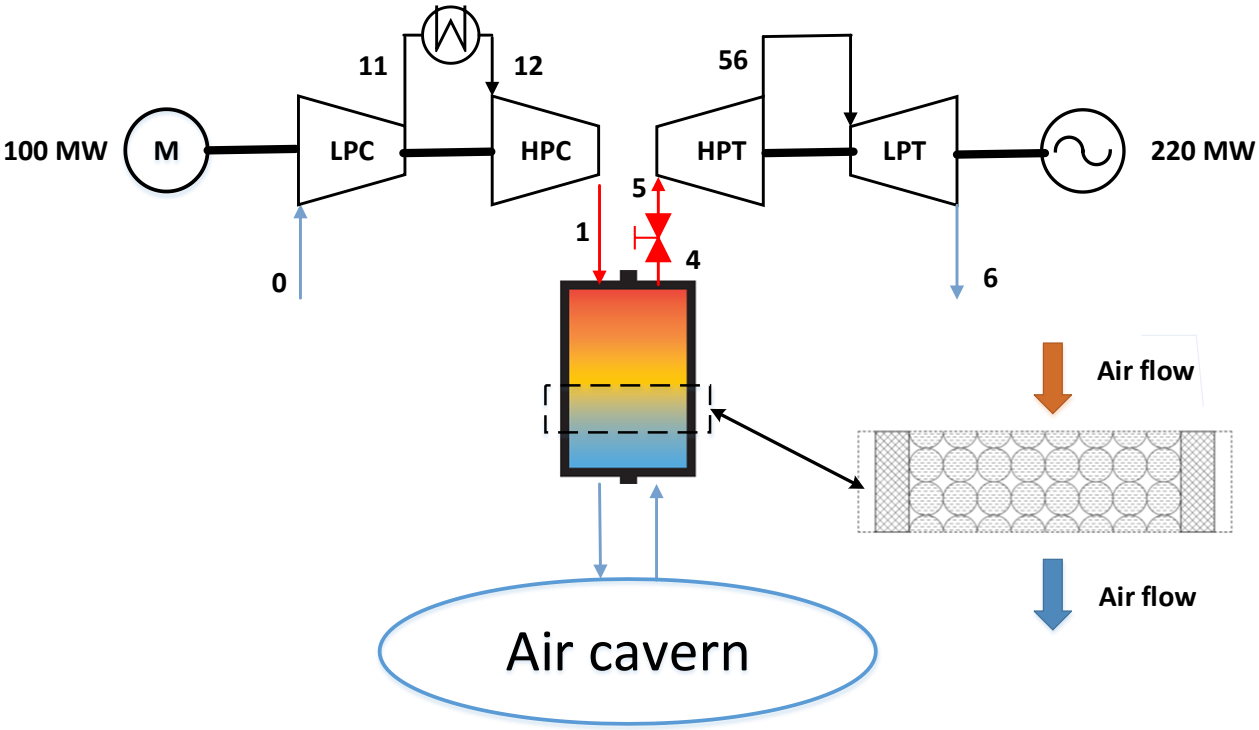

Figure 1: Adiabatic compressed air energy storage (A-CAES) plant with sensible thermal energy storage.

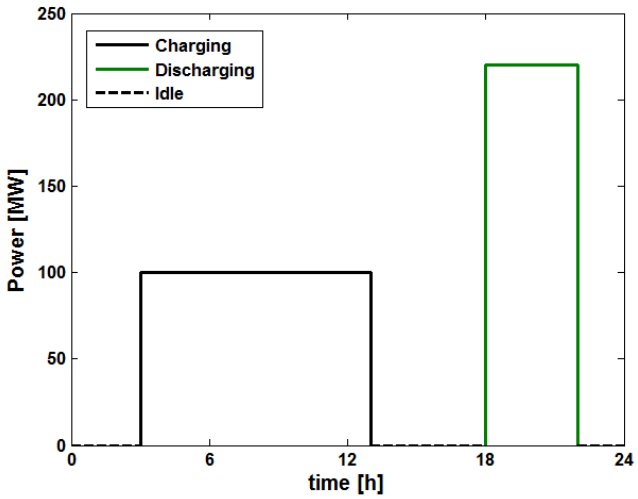

Figure 2: Charge and discharge cycle.

Table 1. Major parameters of A-CAES system

Quantity	Value
Ambient temperature	293.15 K
Ambient pressure	1.01325 bar
Expansion train rated power	220 MW
HP turbine design inlet temperature	905.15 K
HP turbine design inlet pressure	46 bar
HP turbine design expansion ratio	4.18
LP turbine design inlet temperature	655.15 K
LP turbine design inlet pressure	11 bar
LP turbine design expansion ratio	11
Turbines design efficiency	88%
Compression train rated power	100 MW

HP compressor design inlet temperature	480.15 K
HP compressor design compression ratio	8.4
LP compressor design compression ratio	8.4
Cavern volume	230 000 m^3
Cavern min/max pressure	46/72 bar
Cavern wall heat transfer coefficient [43]	$0.02356 + 0.0149\left\|\dot{m}_{in} - \dot{m}_{iout}\right\|^{0.8}$

Table 2. Thermodynamic states for the charging process

State	Temperature [°C]	Pressure [bar]	Enthalpy [kJ/kg]	Entropy [kJ/(kg*K)]	Mass flow rate [kg/s]
0	20	1.01325	300.31	6.87	120
11	309.0	8.5413	588.54	6.93	120
12	207.0	8.5413	482.43	6.73	120
1	632.2	72.0	943.12	6.79	120

Table 3. Thermodynamic states for discharging process

State	Temperature [°C]	Pressure [bar]	Enthalpy [kJ/kg]	Entropy [kJ/(kg*K)]	Mass flow rate [kg/s]
4	632.2	72.0	943.12	6.79	380
5	633.4	46.0	943.12	6.93	380
56	382.3	11.0	666.44	6.98	380
6	134.2	1.01325	408.84	7.17	380

3 Mathematical modelling of A-CAES plant and validation

This section presents the mathematical models for each component of the A-CAES plant depicted in Fig. 1. Each model is first presented separately along with the underlying assumption adopted in the study. The section ends with the description of the solution strategy used to link each sub-model to simulate the whole A-CAES plant. Where not stated explicitly the modelling was performed in Matlab/Simulink 2014 [38].

Compressors

Modelling of low pressure compressor (LPC) and high pressure compressor (HPC) involves mass and energy balance in order to compute temperature of air exiting each stage and the compression work. Isoentropic air outlet temperature was computed as:

$$T_{c,out}^{is} = T_{c,in}\left(\beta_i\right)^{\frac{k-1}{k}} \tag{1}$$

where $\beta_i = \beta_{\mathrm{HPC}}, \beta_{\mathrm{LPC}}$ is the compression ratio of each stage. Actual outlet temperature $T_{c,out}$ was obtained using compressor isoentropic efficiency defined as:

$$\eta_c = \frac{T_{c,out}^{is} - T_{c,in}}{T_{c,out} - T_{c,in}} \tag{2}$$

The power of compressors consumed during charge was evaluate by an energy balance at each compressor neglecting variations in inlet to outlet kinetic energy of air:

131 $$W_c = \dot{m}_c\left(h_{c,out} - h_{c,in}\right) \quad (3)$$

132 In this work we considered off-design performance of compressors during the operation of the A-CAES plant.
133 Off-design are commonly included in models of energy systems, however CAES systems are often studied
134 considering only design conditions [9,11,18]. Such an approach may neglect important dynamic effects when
135 compression train model is included in the whole A-CAES plant model, as we will show in the Results section.
136 We included off-design calculations through compressors characteristic maps [39] that quantify compression
137 ratios β_i and isoentropic efficiency η_i as function of dimensionless flow rate. The characteristic maps were
138 approximated according to [40], namely:

139 $$\beta_i = c_1\left(\dot{G}_c\right)^2 + c_2\dot{G}_c + c_3 \quad (4)$$

140 $$\eta_c = \left[1 - c_4\left(1 - \dot{n}_c\right)^2\right]\left(\dot{n}_c/\dot{G}_c\right)\left(2 - \left(\dot{n}_c/\dot{G}_c\right)\right) \quad (5)$$

141 where $\dot{G}_c$ and $\dot{n}_c$ are the reduced flow rate and the reduced speed, respectively. Figure 3 presents the
142 characteristic maps for the compressors. The definitions for reduced quantities and coefficients of Eqs. 4 and
143 5 are the following ones:

144 $$\begin{aligned} \dot{G}_c &= \left(\dot{m}_c\sqrt{T_{c,in}}/P_{c,in}\right)\Big/\left(\dot{m}_c\sqrt{T_{c,in}}/P_{c,in}\right)_0 \\ \dot{n}_c &= \left(n_c/\sqrt{T_{c,in}}\right)\Big/\left(n_c/\sqrt{T_{c,in}}\right)_0 \end{aligned} \quad (6)$$

145 $$\begin{aligned} c_1 &= \dot{n}_c\Big/\left[p\left(1-\frac{m}{\dot{n}_c}\right)+\dot{n}_c\left(\dot{n}_c-m\right)^2\right] \\ c_2 &= \left(p-2m\dot{n}_c{}^2\right)\Big/\left[p\left(1-\frac{m}{\dot{n}_c}\right)+\dot{n}_c\left(\dot{n}_c-m\right)^2\right] \\ c_3 &= -\left(pm\dot{n}_c-m^2\dot{n}_c{}^3\right)\Big/\left[p\left(1-\frac{m}{\dot{n}_c}\right)+\dot{n}_c\left(\dot{n}_c-m\right)^2\right] \end{aligned} \quad (7)$$

146 Subscript 0 in previous equations denotes design conditions while p = 1.8, m = 1.4 and c_4 = 0.3 [40].

147 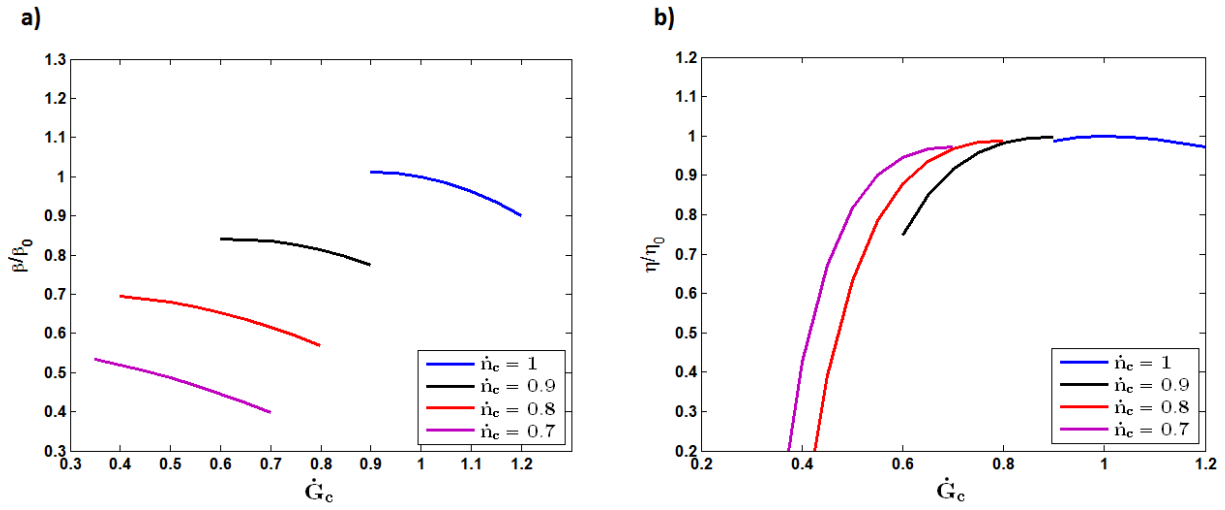

148 Figure 3: Characteristic maps for the compressors. a) Compression ratio vs. reduced flow rate; b) Isoentropic
149 efficiency vs. reduced flow rate.

150 *Turbines*

HP and LP turbine were modelled through mass and energy balance following the same approach adopted for the compressors. Defined the expansion ratio as $\pi_t = p_{in}/p_{out}$, the temperature of air exiting each turbine stage was obtained from the isoentropic temperature and the definition of isoentropic efficiency:

$$T_{t,out}^{is} = T_{t,in} \Big/ (\pi_i)^{\frac{k-1}{k}} \tag{8}$$

$$\eta_t = \frac{T_{t,in} - T_{t,out}}{T_{t,in} - T_{t,out}^{is}} \tag{9}$$

where $\pi_i = \pi_{\mathrm{HPT}}, \pi_{\mathrm{LPT}}$. Finally, the power output was calculated as

$$W_t = \dot{m}_t \left(h_{t,out} - h_{t,in} \right) \tag{10}$$

An improved Flugel formula [40] was used to describe the off-design performance of turbines:

$$\frac{\dot{m}_t}{\dot{m}_{t0}} = \alpha \sqrt{\frac{T_{t0,in}}{T_{t,in}}} \sqrt{\frac{\pi_t^2 - 1}{\pi_{t0}^2 - 1}} \tag{11}$$

$$\frac{\eta_t}{\eta_{t0}} = \left[1 - t(1 - \dot{n}_t)^2 \right] \left(\dot{n}_t / \dot{G}_t \right) \left(2 - \left(\dot{n}_t / \dot{G}_t \right) \right) \tag{12}$$

The definition for reduced flow and reduced speed for turbines are:

$$\begin{aligned} \dot{G}_t &= \left(\dot{m}_t \sqrt{T_{t,in}} / P_{t,in} \right) \Big/ \left(\dot{m}_t \sqrt{T_{t,in}} / P_{t,in} \right)_0 \\ \dot{n}_t &= \left(n_t / \sqrt{T_{t,in}} \right) \Big/ \left(n_t / \sqrt{T_{t,in}} \right)_0 \end{aligned} \tag{13}$$

Fig. 4 illustrates the characteristic maps described by Eqs. (11) and (12).

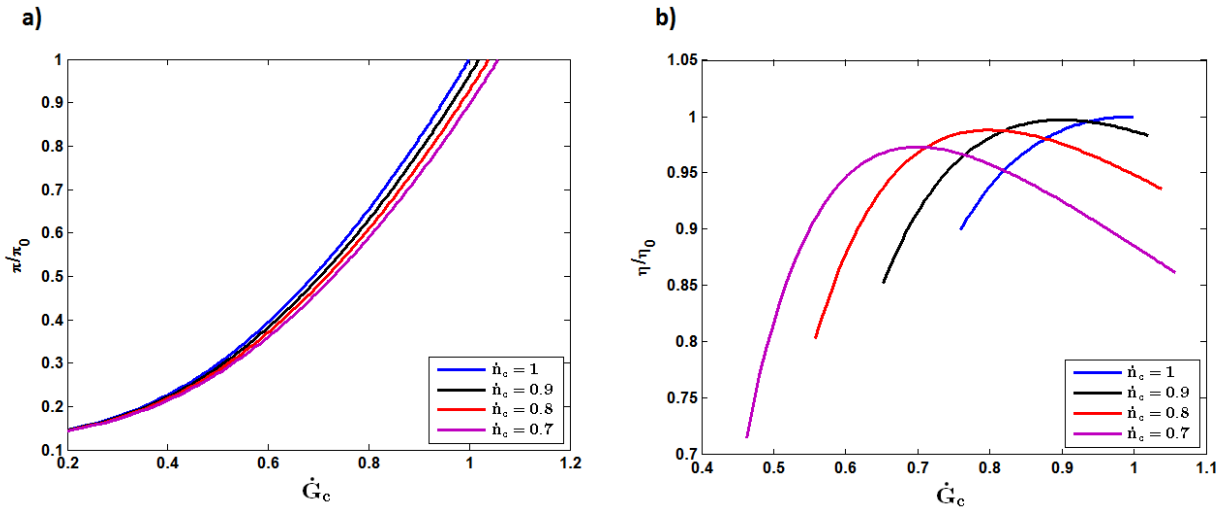

Figure 4: Characteristic maps for the turbines. a) Expansion ratio vs. reduced flow rate; b) Isoentropic efficiency vs. reduced flow rate.

Heat exchanger

The inter-refrigeration heat exchanger between LPC and HPC was modelled using energy balance equation and ε-NTU method [41]; considering a counter flow configuration the effectiveness was calculated as:

$$\varepsilon = \frac{1-\exp\left[-NTU(1-\chi)\right]}{1-\chi\exp\left[-NTU(1-\chi)\right]} \tag{14}$$

where

$$NTU = \frac{UA}{C_{\min}} \quad \chi = \frac{C_{\min}}{C_{\max}} \tag{15}$$

During the charging process effectiveness (14) was evaluated at each instant of time and the actual heat transfer rate was computed as:

$$\Phi_{HEX} = \varepsilon \cdot C_{\min}\left(T_{in,h} - T_{in,c}\right) \tag{16}$$

From heat transfer rate Φ_{HEX} the air outlet temperature (i.e. the HPC inlet temperature) was obtained through the energy balance equation for the heat exchanger.

Compressed air reservoir

We employed a dynamic model to simulate the transient behaviour of temperature of air within the cavern. The model consists of two ordinary differential equations that stem from energy balance and mass balance equations for the air in the cavern [42]:

$$\frac{dT_r}{dt} = \frac{1}{m_r}\left[\left(1-\frac{1}{k}\right)\left(\dot{m}_{in}T_{in} - \dot{m}_{out}T_r\right) + \frac{h_w A_w\left(T_w - T_r\right)}{c_{p,a}}\right] \tag{17}$$

$$\frac{dm_r}{dt} = \dot{m}_{in} - \dot{m}_{out} \tag{18}$$

In equation (17) the first term on the right hand side accounts for energy transfer due to injection/withdraw of air from the cavern under the assumption that air leaves the cavern at the cavern's air temperature. The second term quantifies the heat transfer between air and cavern's walls. Heat transfer coefficient h_w was evaluated as indicated in [43]. Finally, pressure p within the compressed air reservoir was computed with ideal gas law $p/\rho = \bar{R}T$. The model of the cavern was validated against the data gathered by Crotogino et at [8] from the operation of the Huntorf plant. Figure 5 compares the experimental data and the numerical predictions for cavern's temperature and pressure. The experimental data were recorder during a trial cavern discharge of 16 hours. As detailed in [8] the withdrawal rate was 417 kg/s for about 4 hours and then gradually decreased to 150 kg/s at the end of the test. The numerical results match the experimental data for the whole process and correctly predicts the initial decrease of temperature – due to high withdrawal rate – and the final temperature increase caused by heat transfer with the cavern's walls.

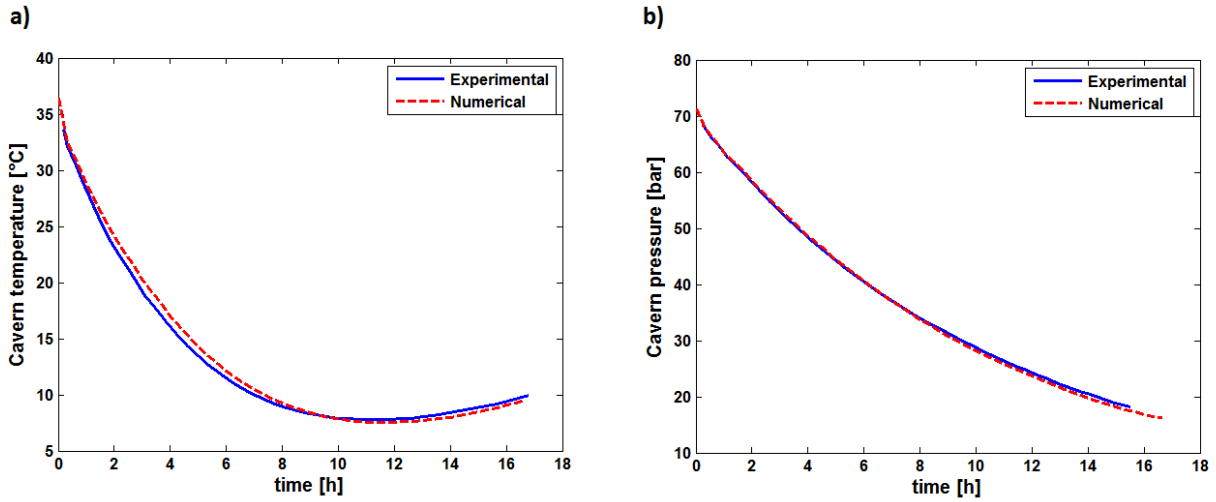

Figure 5: Validation of cavern model; numerical predictions against experimental data from Crotogino F. *et al*. [8].

Packed bed thermal energy storage

We adopted a non-equilibrium model to study heat transfer within the packed bed thermal energy storage (TES). Such an approach has been successfully employed in the literature by various authors [22,23,28,34] and it consists in a set of two energy balance equations, the first one for the air (subscript *a*) in the TES while the second one for the solid filler material (subscript *s*):

$$\varepsilon\rho_a c_{p,a}\frac{\partial T_a}{\partial t}+\varepsilon\rho_a c_{p,a}u_a\frac{\partial T_a}{\partial x}=k_a\frac{\partial^2 T_a}{\partial x^2}-h_v\left(T_a-T_s\right)-U_w\left(T_a-T_0\right) \tag{19}$$

$$\left(1-\varepsilon\right)\rho_s c_{p,s}\frac{\partial T_s}{\partial t}=k_s\frac{\partial^2 T_s}{\partial x^2}+h_v\left(T_s-T_a\right) \tag{20}$$

In Eqs. 19 and 20 we assumed – as commonly done in the literature [22,23,28,34] – one dimensional heat transfer along the packed bed length *x*. Void fraction ε of the bed was evaluated as function of the ratio particle diameter d_p to packed bed diameter D [34]:

$$\varepsilon=0.375+0.17\frac{d_p}{D}+0.39\left(\frac{d_p}{D}\right)^2 \tag{21}$$

Air velocity u_a was evaluated at each instant of time starting from compressor mass flow rate, during charge, and turbine mass flow rate during discharge. Uniform velocity throughout the TES transversal cross section was considered. The thermal conductivity k_s of the bed was evaluated by means of the Zehner-Bauer–Schlunder model [44].

The second term on the right hand side of Eq. (20) accounts for the heat transfer between the air and the solid particles in the thermal storage system. The volumetric heat transfer coefficient h_v was computed using the Coutier's correlation [25,34]:

$$hv=700\left(\frac{G}{d_p}\right)^{0.76} \tag{22}$$

where G is the mass flux (kg s^{-1} m^{-2}) flowing through the packed bed thermal storage system. The last term on the right hand side of Eq. (20) quantifies the heat loss toward the ambient at temperature T_0. We attributed the heat loss entirely to the fluid phase (Eq. 20) since separate correlations are not available in the literature and experiment cannot distinguish properly between phases [34]. Heat transfer coefficient U_w was determined considering heat transfer through a multi-layer cylindrical wall [41]. Table 4 summarizes the major parameters of the TES system. The diameter D and height H of the TES system were obtained through a preliminary design on the basis of data in Tables 1 and 2 together with charge/discharge cycle of Fig. 2. Such data allows to estimate heat to be stored and thus the geometrical dimensions of the TES system. Such dimensions are in line with those reported in [19, 45], although other arrangements, such as multiple TES in parallel/series could be also considered.

Table 4. Input parameters for TES model

Property	Formulation
ρ_s (kg/m^3)	2911 [22]
$c_{p,s}$ (J/kg K)	$A\left(B + CT + B/T^2\right)$ [47]
k_s (W/m K)	Zehner-Bauer–Schlunder model [44]
d_p (m)	0.02 [34]
H (m)	22
D (m)	20

To validate the model the numerical predictions were compared with experimental results obtained by Meier et al. [26]. The researchers studied a lab scale packed bed thermal energy storage and recorded temperature along the packed bed during charge. The major parameters of the experimental set up considered by Meier et al. are available in [26,34]. Our packed bed model, comprising Eqs. 19-22, was run in standalone mode using mass flow rate and thermos-physical properties available in [26,34] as input parameters. Clearly, in our validation study we adopted the same packed bed diameter D and length L considered by Meier et al [26].

Figure 6 compares the temperature profile along the TES predicted by our model and the experimental data from [26] at different instants of time. The comparison demonstrates that the model is capable of predicting both temperature and position of the thermal front with good accuracy. Discrepancy between experiments and simulation can be attributed to the small ratio $D/d_p = 7.5$ considered in [26]: when particle diameter d_p is relatively large compared to packed bed diameter D a non-negligible fraction of the air mass flow rate passes near the walls of the packed bed, thus it does not contribute to heat transfer with the filling material. Therefore, the accuracy of the model, which is already satisfactory for a small lab scale device, will further improve when a full scale system is considered.

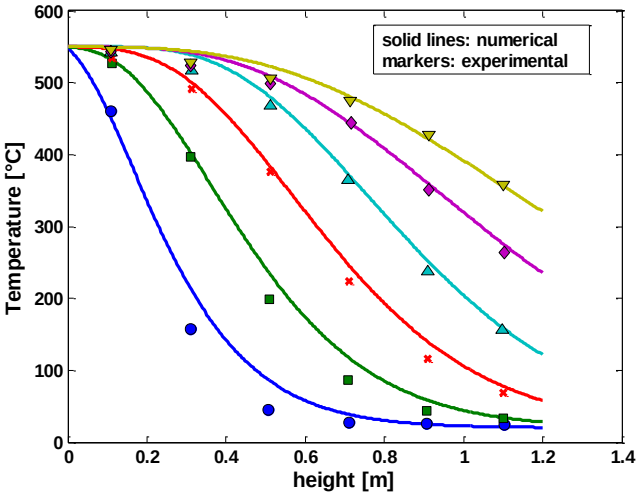

Figure 6: Validation of packed bed model; Numerical predictions against experimental data from Meier et al. [26].

Performance indicators

The round trip efficiency and the thermal storage efficiency were used to assess the performance of the whole A-CAES plant and the thermal energy storage system. The round trip efficiency for each charge/discharge cycle was calculated as:

$$\eta_{cycle} = \frac{E_{out}}{E_{in}} = \frac{\int_0^{\Delta t_d} W_t dt}{\int_0^{\Delta t_c} W_c dt} \tag{23}$$

The time integration is performed over each charging period (Δt_c) and discharging period (Δt_d).

The performance of the TES system was assessed through the thermal storage efficiency defined as follows:

$$\eta_{th} = \frac{\int_0^{\Delta t_d} \dot{m}_t (h_4 - h_0) dt}{\int_0^{\Delta t_c} \dot{m}_c (h_1 - h_0) dt} \tag{24}$$

Where h_4 is the specific enthalpy of air at the outlet of the TES system during discharging while h_1 is the specific enthalpy of air the inlet of TES system during charging.

A-CAES plant simulations

The previous equations were implemented in Matlab/Simulink to simulate the entire A-CAES plant. The block diagram of Fig. 7 shows how the sub-systems interact during calculation for charging and discharging processes. The equations were solved using 4th order Runge Kutta method with variable time step. Two distinct sub-sets of equations were solved depending if the plant operates in charge or discharge mode. The interactions between the components of the plant lead to two sub-sets of coupled equations, as clarified by the process flow indicated by the arrows in Fig. 7. The arrows in the figure indicates which components (blocks), and therefore the corresponding equations, involved during simulation of charge and discharge processes. Separate blocks exchanging information (mass flow rate, pressure and temperature) at each instant of time were implemented in Simulink.

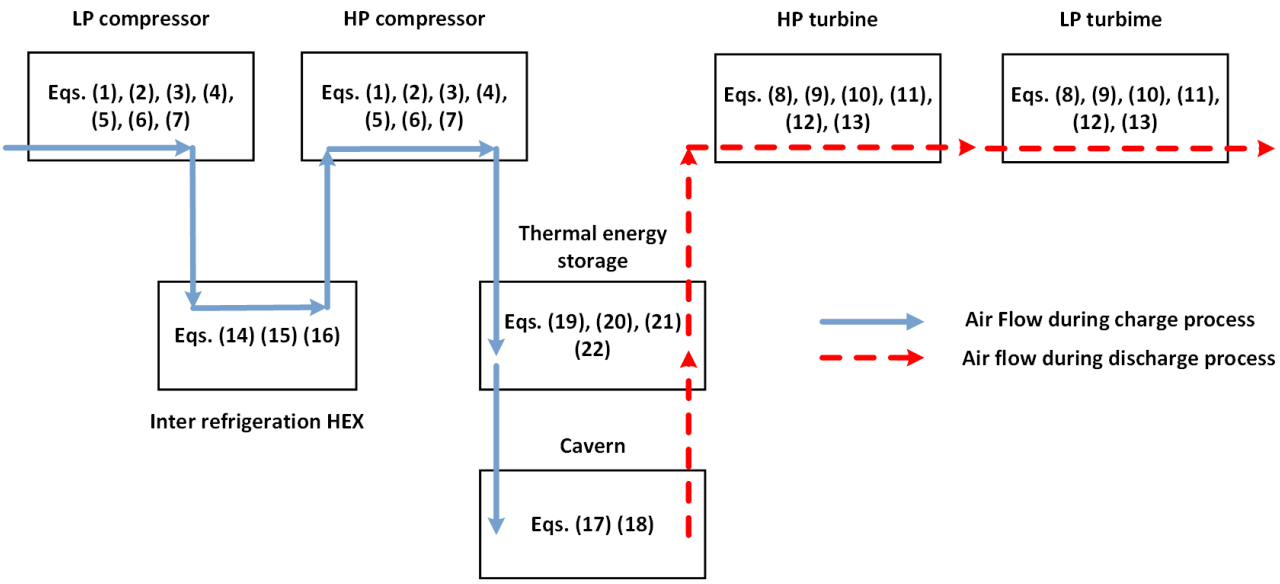

Figure 7: Block diagram for the whole A-CAES plant model.

4 Results and Discussion

The simulations provide results for each component depicted in Fig. 1 for 30 consecutive charge/discharge cycles. A subset of these results are shown in Fig. 8 to clarify the plant operation; detailed results for each component of the plant are presented in the following subsections. Fig. 8a plots the power input/output for the A-CAES plant. Both compression train and expansion train operate around the corresponding rated power (100 MW/220MW); the variations in compression power and expansion power during charge stage and discharge stage are due to off-design operating conditions which will be detailed in sections 4.2 and 4.3. Fig. 8b shows the state of charge for the thermal store and the compressed air reservoir. The stored thermal energy and the air pressure show a similar time pattern, since both follow charge/discharge cycles; 940 MWh_{th} are stored in the TES on average (see Table 5) while TES efficiency, as defined by Eq. (24), is 93%. Cavern pressure spans the range 48-71 bar. Pressure variation occurs also during idle stage: after each discharge process cavern pressure increases from ~ 48 bar to about 50 bar due to heat transfer from cavern walls to compressed air, the latter being relatively cold because of the withdraw process during discharge. A similar effect was also pointed out in [46]. During idle after each charge, the pressure in the cavern slightly drops before the next discharge. In this case heat flows from the compressed air to the cavern wall cooling the mass of air in the cavern and thus leading to a reduction of pressure.

Figure 9 displays the round trip efficiency and thermal storage efficiency over 30 cycles. Both efficiencies reach a stable value after an initial increase during the first operating cycles. The key quantity here is the efficiency of the thermal storage system: as soon as TES starts to operate in an effective way the overall performance significantly improves, which shows how relevant is to integrate carefully the thermal storage with the remaining part of the system. Maximum TES efficiency occurs when static cycling operating conditions are established in the thermal storage as explained in the next section. Clearly, the predicted value for of roundtrip efficiency are affected by the value of parameters used in the model. We adopted, whenever possible, values commonly used in the CAES literature and that led to accurate results when compared with experimental data. We estimated, by varying turbine isoentropic efficiency between 0.8 and 0.88, that changes in roundtrip efficiency stays within ±10%.

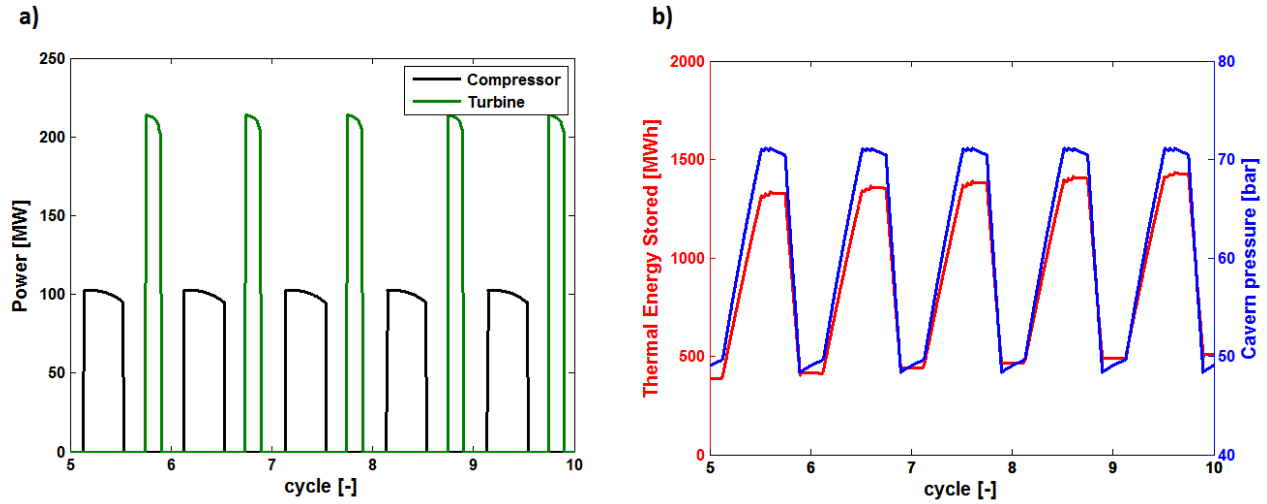

Figure 8: A-CAES plant performance between 5th and 10th operation cycle. a) Compression train power during reservoir charge and turbine power output during discharge. b) Thermal energy stored in the sensible TES (left axis) and reservoir pressure variation (right axis) due to injection/withdraw of compressed air.

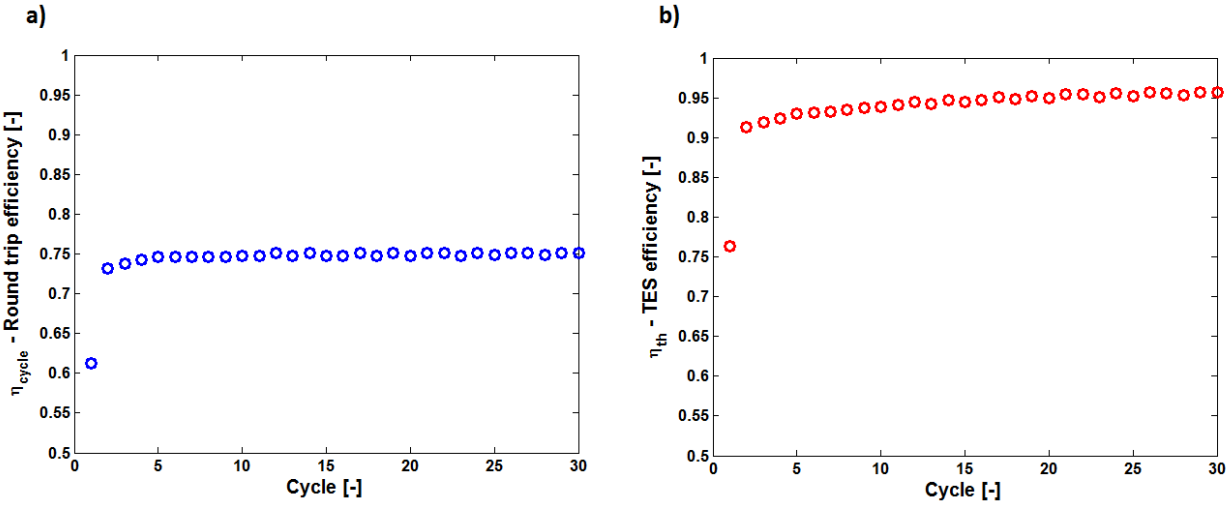

Figure 9: Efficiency of A-CAES plant. a) Round trip efficiency according to Eq. (23); b) Efficiency of the thermal energy storage system (Eq. 24).

Table 5. A-CAES performance for full load charging/discharging

Quantity	Value
Number of cycles (-)	30
Round trip efficiency η_{cycle} (-)	74%*
Total output energy (MWh_e)	22100
Charge time (h)	9.1*
Discharge time (h)	3.3*
Thermal energy stored (MWh_{th})	940*
Thermal energy storage efficiency η_{th} (-)	93%*

* Averaged value over 30 cycles

4.1 Thermal energy storage (TES) system

Figure 10 presents the temperature profile within the TES system and shows how the temperature profile varies from cycle to cycle. Figure 10a shows temperature after charge (t = 16h within each cycle). Two key features

should be noticed: the position of the thermal front and how the temperature evolves, after a sufficient number of cycles, toward a cycling stationary profile. After cycle 1 the temperature shows a thermal front around x = 11 m that extends for about 10% of the TES length. The ideal operation of the TES system, as illustrated in [28,31], would preserve the thermal front as sharp as possible from cycle to cycle, while each charge/discharge would consist in such sharp front travelling back and forth from $x = 0$ to $x = H$. Thermal degradation of the front [28] prevents a practical implementation of the ideal TES operation, in fact after 5 cycles thermal front broadens up to 50% of TES length. Therefore, the thermal store actually operates very similarly to a regenerator: air is gradually cooled during charge, while it is gradually heated – from TES inlet to TES outlet – during discharge. Such an operation mode leads to stationary cycling operating conditions, where two stationary temperature profiles occur after charge and discharge (see cycle 30 in Fig. 10). Stationary profile slightly decreases from $x = 0$ m to $x = 10$ m due to increase in air outlet temperature from HP compressor during charge. During discharge, air withdrawn from the cavern is slightly above ambient temperature; this causes the hump at $x = 15$ m illustrated in Fig. 10b.

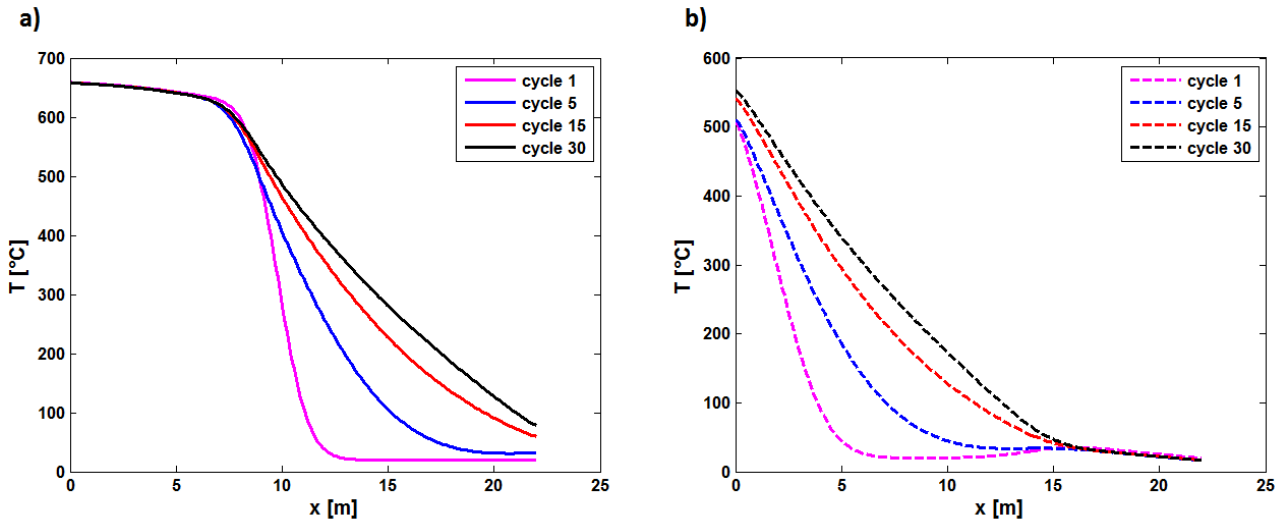

Figure 10: Temperature profile along the length of the thermal energy storage (TES) system. a) Temperature profiles after charging; b) Temperature profiles after discharge. Cycling operating conditions establish after 20 cycles of charging/discharging.

The time evolution of air at the outlet of TES system – corresponding T_4 in Fig. 1 – is presented in Fig 11. The outlet temperature stays within a range of 20°C for about 67% of the discharge time; such an operating condition corresponds to the time necessary for the flat portion of the TES temperature profile ($x < 10$ m in Fig. 10a) to leave the thermal store during discharge. During the last stage of discharge the outlet temperature drops of about 15%, as the degraded thermal front exits the thermal store. A more marked drop occurs during the first cycles because stationary temperature profile is not established yet in the TES system. Air outlet temperature from the packed bed storage coincides with the HP turbine inlet temperature; thus, any variation of T_4 from design point detriments the performance and efficiency of the expansion train, as explained in Sect. 4.3. These results presented here can help CAES operators to conceive optimal operating strategy to reduce such undesired off-design conditions.

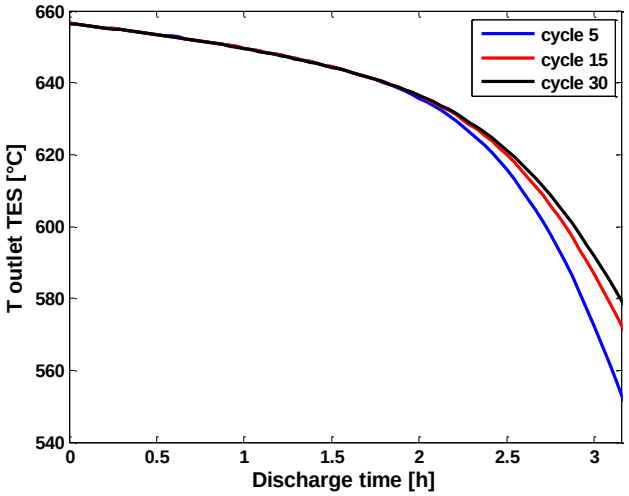

Figure 11: Temperature profile along the length of the thermal energy storage (TES) system. a) profiles after charging; b) profiles after discharge. Cycling operating conditions establish after 20 cycles of charging/discharging.

4.2 Compression train

The performance of low pressure compressor (LPC) and high pressure compressor (HPC) significantly depart from nominal condition, as both compressors operate off-design during charging. In fact, the pressure of air in the cavern constantly increases during charge, causing an increase also in the total pressure ratio experienced by the compressor train. As a consequence, compressors' operating point moves along characteristic curve (Fig. 3) from low to high pressure ratio. Figure 12 lucidly summarizes how the compression train operates during charge. At the beginning of charging the LPC performs the majority of the compression work as LP compression ratio is ~ 16% larger than the HP one. As pressure in the cavern rises, both β_{LPC} and β_{HPC} increment up to the corresponding design values, which is achieved only at the end of charge. As charging starts $\beta_{LPC} = 7.6$ and $\beta_{LPC} = 6.5$, thus LPC compression ratio and HPC compression ratio are respectively 10% and 22% lower that the design value. As a result, the minimum isoentropic efficiency of compressors occurs at the begin of each charge as shown in Fig. 12a. Figure 12b shows that at the end of charging the HP compressor outlet temperature is 660°C while – from Fig 11 – we found at the beginning of discharge air leaves the TES systems at 656°C. Such a difference between the two temperatures is due to finite heat transfer between the air stream and the rocks within the TES. However, the difference is very limited due to the good thermal contact (large heat transfer area) between air and TES filling material.

The compression power shows a maximum around t = 2h which can be explained from the behaviour of mass flow rate (Fig. 13) and compression ratios (Fig. 12b). The combination of decreasing trend for $\dot{m}_c$ with an increasing trend for β_{LPC}, β_{HPC} brings a maximum in compression power W_c (Eq. 3). The mass flow rate monotonically decreases during charge because the operating point of compressors (Fig. 3) shifts from low compression ratios, so high mass flow rate $\dot{G}_c$, to high compression ratio and lower mass flow rate. On the other hand, the compression ratio monotonically increases during charge as cavern pressure rises.

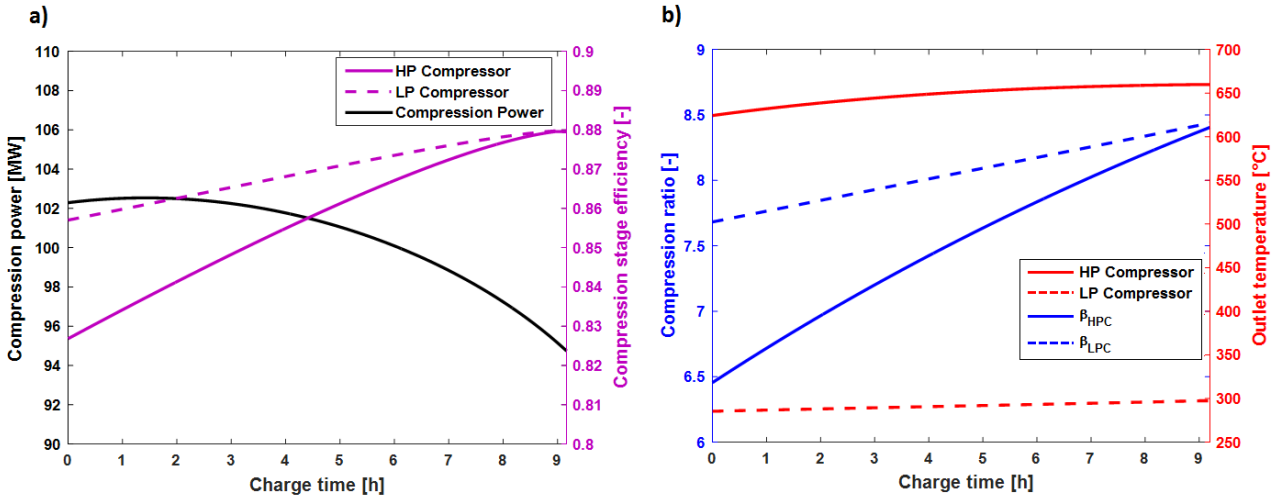

Figure 12: Compression train performance during charge. a) Compression power and isoentropic efficiency of high pressure and low pressure compressors. b) Compression ratio and air outlet temperature for high and low pressure compressors. Compressor train operates under off-design conditions except at the end of the charging process.

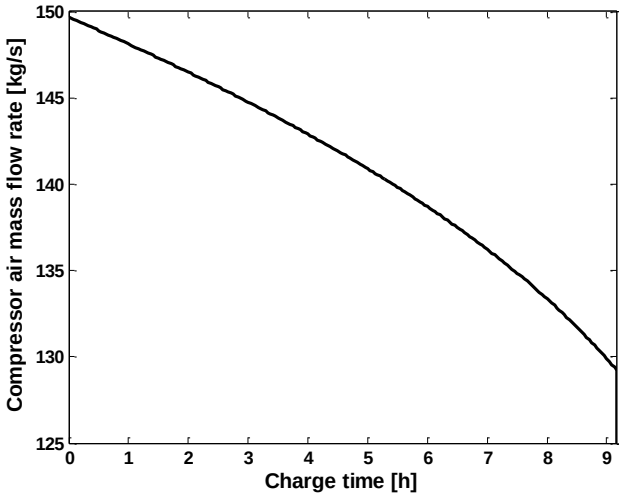

Figure 13: Compressor air mass flow rate during charge. During charge compression ration increases (Fig. 12b) consequently mass flow rate diminishes as compressor operation point moves along the characteristic curve (Fig. 3).

4.3 Expansion train

The expansion train operates under constant expansion ratio – due to the throttling valve (Fig. 1) – but with variable inlet temperature of air coming from the thermal energy storage system (Fig. 11). As a results departure from design condition are limited in comparison with the compression train, as illustrated in Fig. 14. Both high pressure turbine (HPT) and low pressure turbine (LPT) perform at design isoentropic efficiency for the entire discharge process. The power output drops of about 5% during discharge due to a combined effects of decrease in inlet temperature (Fig. 11) and variation of the turbine mass flow rate (Fig. 15). Although the turbine mass flow rate increases, as depicted in Fig. 15a, the drop in inlet temperature (Fig 11) dominates the behaviour of turbine power, resulting in a reduction of power output from the A-CAES plant. This shows how important is to conceive and operate the thermal storage system in an optimal way, since TES performance reverberate onto the global performance of the plant. Variations of the turbine mass flow rate are also caused

by reduction of air inlet temperature: according to the Flügel formula (Eq. 11) at constant expansion ratio we have $\dot{m}_t \propto 1/\sqrt{T_{inlet}}$. Finally, the decrease of the air outlet temperature from HPT and LPT shown in Fig. 15b stems directly from the reduction in the inlet temperature.

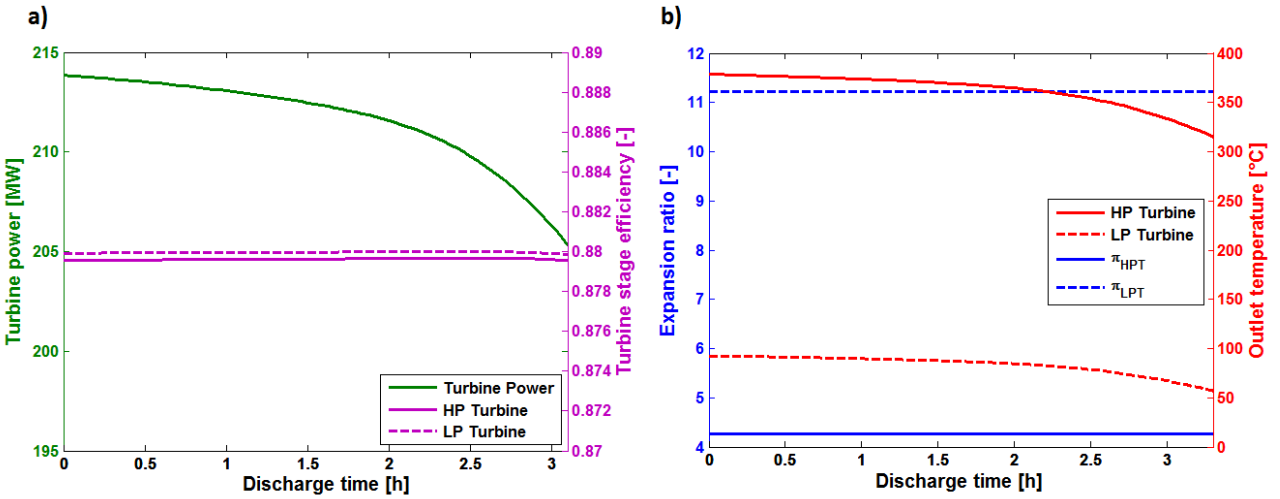

Figure 14: Expansion train performance during discharge. a) Turbine power and isoentropic efficiency of high pressure and low pressure turbine. b) Expansion ratio and air outlet temperature for high and low pressure turbine. Expansion train operates near design conditions for most of discharge process because of constant inlet pressure.

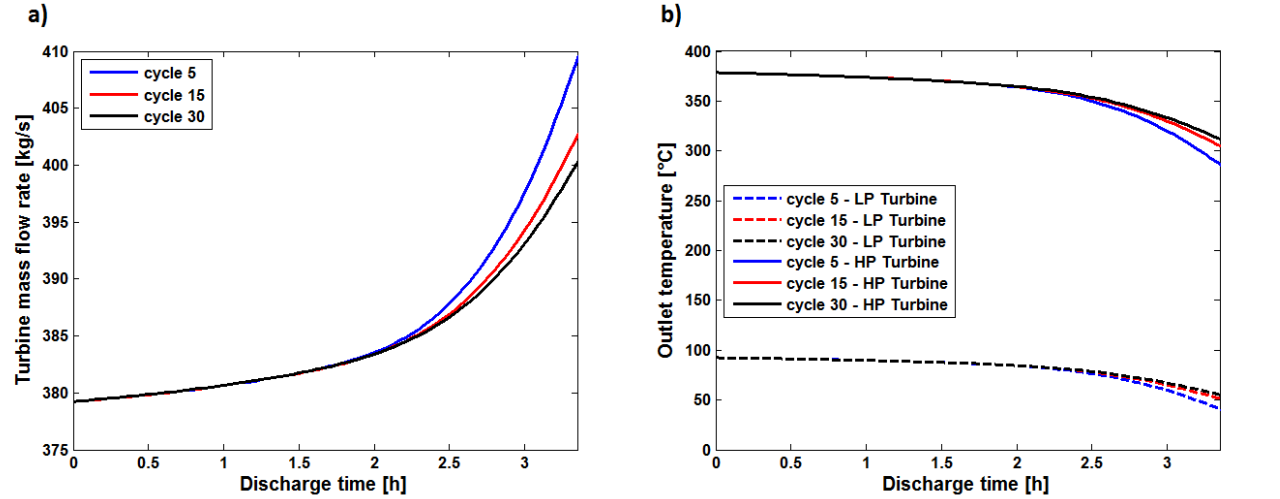

Figure 15: Variation of turbine operation over charge/discharge cycles. a) Turbine mass flow rate b) Air outlet temperature from low pressure and high pressure turbine. Variation of turbine inlet temperature (Fig. 11) leads to increase of flow rate due off-design conditions.

4.4 Partial load operation

The operation of CAES systems for peak shaving, minute reserve, or compensation of fluctuation in wind power likely involves partial load operation during discharging [37]. The model we developed allows us to study A-CAES performance for partial load operating cycle. We considered the cycle of Fig. 16 to show how partial load conditions may detriment A-CAES performance. In the view of peak shaving operation we considered a discharge cycle that last four hours (as in case of Fig. 2) but at three different loads. This mimics operating condition that may realistically occurs, as presented in [8,43]. The power output is controlled by

adjusting the inlet pressure for HP turbine by throttling air flow from the cavern. Table 6 summarizes the results for this operation mode.

Figure 17 shows the performance indicators for A-CAES plant and TES system. Round trip efficiency detriments due to smaller power output while TES is marginally affected by partial-load operation which causes variation of air flow through the TES as detailed below. As the inlet pressure varies with the load, HP and LP expansion ratios adjust accordingly (Fig 18). Maximum relative variation of π_{HPT} is nearly 40% which causes non-negligible changes in the corresponding isoentropic efficiency. The outlet temperature from the turbine stages (Fig. 18a) varies following the changes in the expansion ratios. The outlet temperature drops toward the end of discharging cycle since the temperature of air from TES reduces, as previously illustrated for Fig. 11. Cycle-to-cycle variations can be seen in Fig. 19, as stationary temperature profile establishes within the thermal energy storage system.

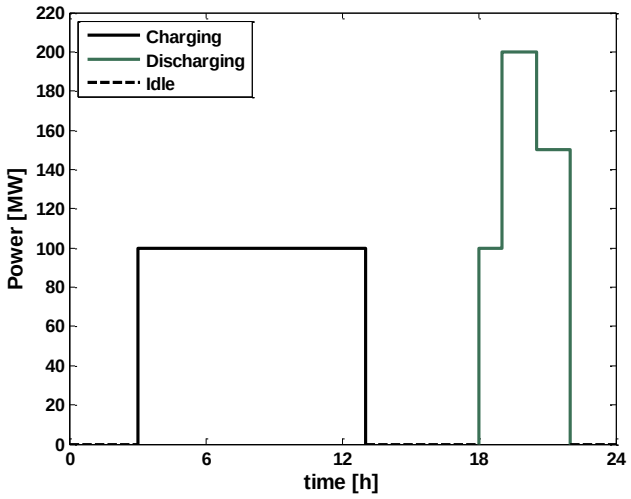

Figure 16: Charge and discharge cycle – partial load case.

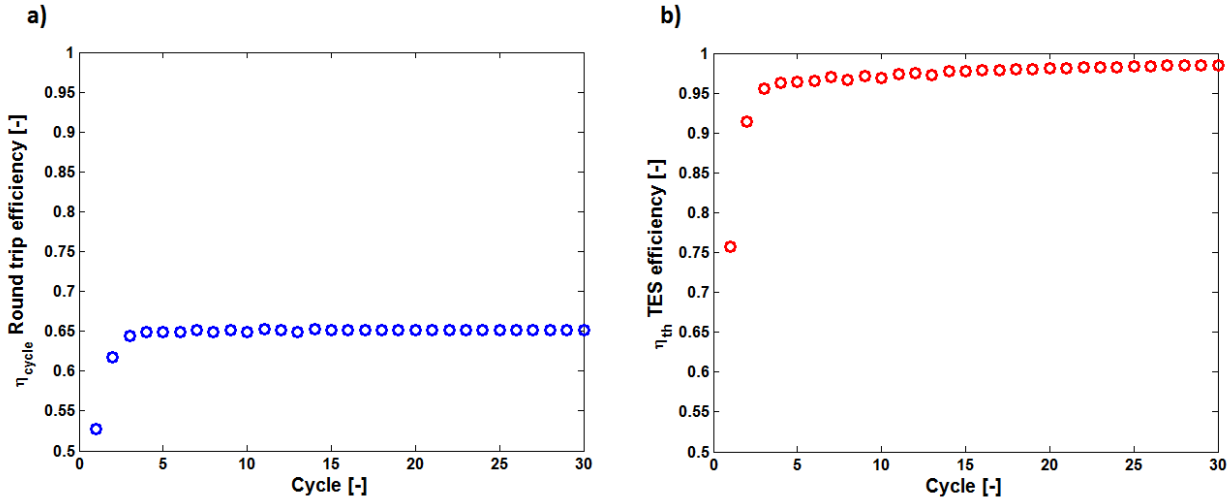

Figure 17: Efficiency of A-CAES plant under partial load operation. a) Round trip efficiency according to Eq. (23); b) Efficiency of the thermal energy storage system (Eq. 24).

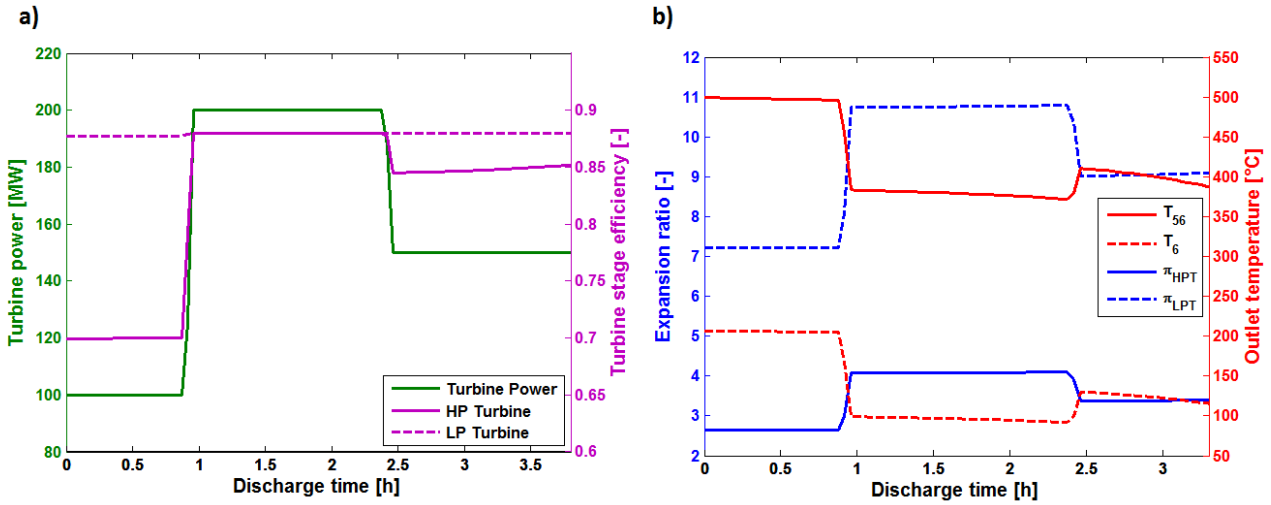

Figure 18: Expansion train performance during partial load discharge. a) Turbine power and isoentropic efficiency of high pressure and low pressure turbine. b) Expansion ratio and air outlet temperature for high and low pressure turbine.

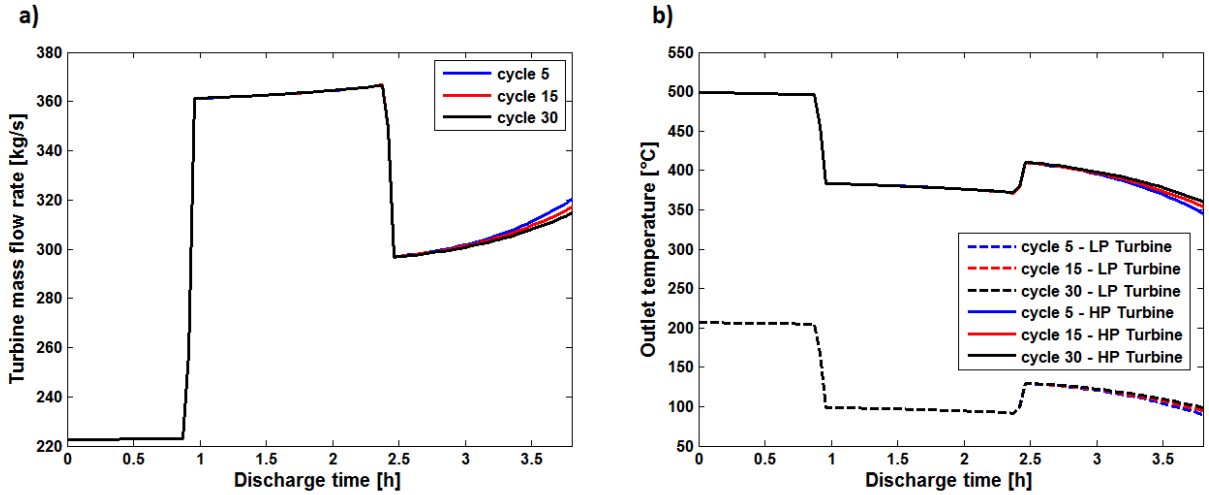

Figure 19: Variation of turbine operation over charge/discharge cycles at partial load. a) Turbine mass flow rate b) Air outlet temperature from low pressure and high pressure turbine.

Table 6. A-CAES performance for partial load operation

Quantity	Value
Number of cycles (-)	30
Round trip efficiency η_{cycle} (-)	64%*
Total output energy (MWh_e)	18900
Charge time (h)	8.5*
Discharge time (h)	3.8*
Thermal energy stored (MWh_{th})	860*
Thermal energy storage efficiency η_{th} (-)	96%*

* Averaged value over 30 cycles

5 Conclusions

In this paper we developed for the first time a fully dynamic and off-design performance model of an A-CAES plant with a packed bed thermal energy storage (TES) system. This was possible by integrating together

algebraic and differential sub-models that detail the transient features of the thermal storage, the cavern, and the compression/expansion stages, which is a novelty proposed in this work.

Both design and off-design charging/discharging cycles were studied for the specific A-CAES plant considered. The results indicate that under nominal charging/discharging a round trip efficiency exceeding 70% can be achieved when TES efficiency rises above 90%. The link between device performance with plant performance was elucidated. In fact we can conclude that: i) maximum round trip efficiency occurs when cycling stationary temperature profiles establishes in the packed bed TES; ii) A-CAES performance detriments toward the end of each discharging cycle due to degradation of the thermal front within the thermal store; iii) reduction of air outlet temperature from TES system causes the turbine to operate in off-design conditions leading to an increase of flow rate; iv) the compressors operate under strong off-design conditions which also affect temperature profile in thermal storage system.

In summary, we showed that the linking device dynamic performance with system performance is a necessity, since modern energy storage systems present a strong tendency toward transient operation. We achieved such a goal, for the first time for A-CAES, with the work presented in this paper.

Acknowledgments

The authors would like to thank the research grant support from Engineering and Physical Sciences Research Council, UK - Next Generation Grid Scale Thermal Energy Storage Technologies (NexGen-TEST) (EP/L014211/1)

References

[1] 2015 key world energy statistics. IEA - International Energy Agency. https://www.iea.org/publications/freepublications/publication/key-world-energy-statistics-2015.html [accessed 05.01.16]

[2] IPCC, 2014: Climate Change 2014: Synthesis Report. Contribution of Working Groups I, II and III to the Fifth Assessment Report of the Intergovernmental Panel on Climate Change [Core Writing Team, R.K. Pachauri and L.A. Meyer (eds.)]. IPCC, Geneva, Switzerland, 151 pp.

[3] Energy Technology Perspective 2014 Harnessing Electricity's Potential. IEA - International Energy Agency. http://www.iea.org/Textbase/npsum/ETP2014SUM.pdf [accessed 05.01.16].

[4] Xing Luo, Jihong Wang, Mark Dooner, Jonathan Clarke. Overview of current development in electrical energy storage technologies and the application potential in power system operation. Applied Energy 2015; 137:511–536.

[5] Haisheng Chen, Thang Ngoc Cong, Wei Yang, Chunqing Tan, Yongliang Li, Yulong Ding. Progress in electrical energy storage system: A critical review. Progress in Natural Science 2009; 19:291–312

[6] Budt M, Wolf D, Span R, Yan J. A review on compressed air energy storage: Basic principles, past milestones and recent developments. Applied Energy 2016; 170: 250–268

[7] Barnes F.S., Levine J.G. Large energy storage system handbook. (2011) CRC Press Tylor & Francis Group. Boca Raton FL.

[8] Crotogino F, Mohmeyer K-U, Scharf R. Huntorf CAES: more than 20 Years of Successful Operation. In: Proceedings of SMRI Spring Meeting, Orlando, Florida, USA; 15–18 April 2001.

[9] Niklas Hartmann, O. Vöhringer, C. Kruck, L. Eltrop. Simulation and analysis of different adiabatic Compressed Air Energy Storage plant configurations. Applied Energy 2012; 93:541–548.

[10] Ibrahim H, Ilinca A, Perron J. Energy storage systems – characteristics and comparisons. Renew Sust Energ Rev 2008; 12:1221–50.

[11] Grazzini G., Milazzo A. A Thermodynamic Analysis of Multistage Adiabatic CAES. Vol. 100, No. 2, February 2012 | Proceedings of the IEEE.

[12] Grazzini G., Milazzo A. Thermodynamic analysis of CAES/TES systems for renewable energy plants. Renewable Energy 2008; 33:1998–2006

[13] William F. Pickard, Nicholas J. Hansing, and Amy Q. Shen. Can large-scale advanced-adiabatic compressed air energy storage be justified economically in an age of sustainable energy? Journal of Renewable and Sustainable Energy 2009; 1:033102 doi: 10.1063/1.3139449

[14] Luo X, Wang J, Krupke C, Wang Y, Sheng Y, Li J, Xu Y, Wang D, Miao S, Chen H. Modelling study, efficiency analysis and optimisation of large-scale Adiabatic Compressed Air Energy Storage systems with low-temperature thermal storage. Applied Energy 2016; 162: 589-600.

[15] Yuan Zhang, Ke Yang, Xuemei Li, Jianzhong Xu. The thermodynamic effect of thermal energy storage on compressed air energy storage system. Renewable Energy 2013; 50:227-235.

[16] Ke Yang, Yuan Zhang, Xuemei Li, Jianzhong Xu. Theoretical evaluation on the impact of heat exchanger in Advanced Adiabatic Compressed Air Energy Storage system. Energy Conversion and Management 2014; 86:1031–1044.

[17] Pan Zhao, Mingkun Wang, Jiangfeng Wang, Yiping Dai. A preliminary dynamic behaviors analysis of a hybrid energy storage system based on adiabatic compressed air energy storage and flywheel energy storage system for wind power application. Energy 2015; 84:825-839

[18] Zuogang Guo, Guangyi Deng, Yongchun Fan, Guangming Chen. Performance optimization of adiabatic compressed air energy storage with ejector technology. Applied Thermal Engineering 2016; 94:193–197

[19] A. Kéré, V. Goetz, X. Py, R. Olives, N. Sadiki. Modeling and integration of a heat storage tank in a compressed air electricity storage process. Energy Conversion and Management 2015; 103:499–510

[20] Peiwen Li, Jon Van Lew, Wafaa Karaki, Cholik Chan, Jake Stephens, Qiuwang Wang. Generalized charts of energy storage effectiveness for thermocline heat storage tank design and calibration. Solar Energy 2011; 85:2130–2143.

[21] Peiwen Li, Jon Van Lew, Cholik Chan, Wafaa Karaki, Jake Stephens, J.E. O'Brien. Similarity and generalized analysis of efficiencies of thermal energy storage systems. Renewable Energy 2012; 39:388-402.

[22] G. Zanganeh, A. Pedretti, S. Zavattoni, M. Barbato, A. Steinfeld. Packed-bed thermal storage for concentrated solar power –Pilot-scale demonstration and industrial-scale design. Solar Energy 2012; 86:3084–3098.

[23] G. Zanganeh, A. Pedretti, A. Haselbacher, A. Steinfeld. Design of packed bed thermal energy storage systems for high-temperature industrial process heat. Applied Energy 2015; 137:812–822.

[24] P. Klein, T.H. Roos, T.J. Sheer. Parametric analysis of a high temperature packed bed thermal storage design for a solar gas turbine. Solar Energy 2015; 118:59–73.

[25] Coutier, J.P., Farber, E.A. Two applications of a numerical approach of heat transfer process within rock beds. Sol. Energy 1982; 29:451–462.

[26] Meier A., Winkler C., Wuillemin D. Experiment for modelling high temperature rock bed storage. Sol. Energy Mater. 1991; 24:255–264.

[27] Markus Hänchen, Sarah Brückner, Aldo Steinfeld. High-temperature thermal storage using a packed bed of rocks e Heat transfer analysis and experimental validation. Applied Thermal Engineering 2011; 31: 1798-1806

[28] Hitesh Bindra, Pablo Bueno, Jeffrey F. Morris, Reuel Shinnar. Thermal analysis and exergy evaluation of packed bed thermal storage systems. Applied Thermal Engineering 2013; 52:255-263.

[29] Hao Peng, Rui Li, Xiang Ling, Huihua Dong. Modeling on heat storage performance of compressed air in a packed bed system. Applied Energy 2015; 160:1–9

[30] Ryan Anderson, Liana Bates, Erick Johnson, Jeffrey F. Morris. Packed bed thermal energy storage: A simplified experimentally validated model. Journal of Energy Storage 2015; 4:14–23

[31] White A. Loss analysis of thermal reservoirs for electrical energy storage schemes. Applied Energy 2011; 88:4150–4159.

[32] Lukas Heller, Paul Gauche. Modeling of the rock bed thermal energy storage system of a combined cycle solar thermal power plant in South Africa. Solar Energy 2013; 93:345–356.

[33] González I, Pérez-Segarra C.D, Lehmkuhl O, Torras S, Oliva A. Thermo-mechanical parametric analysis of packed-bed thermocline energy storage tanks. Applied Energy 2016; 179: 1106–1122

[34] Nicolas Mertens, Falah Alobaid, Lorenz Frigge, Bernd Epple. Dynamic simulation of integrated rock-bed thermocline storage for concentrated solar power. Solar Energy 2014; 110:830–842

[35] RWE power. ADELE – Adiabatic compressed air energy storage for electricity supply. http://www.rwe.com/web/cms/mediablob/en/391748/data/364260/1/rwe-powerag/innovations/adele/Brochure-ADELE.pdf.

[36] http://www.alacaes.com/ [accessed 6.01.16]

[37] Pan Zhao, Lin Gao, Jiangfeng Wang, Yiping Dai. Energy efficiency analysis and off-design analysis of two different discharge modes for compressed air energy storage system using axial turbines. Renewable Energy 2016; 85:1164-1177

[38] MATLAB (2014). The Language of Technical Computing, Matlab 2014a, The MatWorks, Inc., Natick, MA.

[39] S. L. Dixon C. A. Hall. Fuid Mechanics and Thermodynamics of Turbomachinery. (2014) Seventh Edition Butterworth-Heinemann, Elsevier. Oxford, UK.

[40] N. Zhang, R.X. Cai, Analytical solutions and typical characteristics of part-load performance of single shaft gas turbine and its cogeneration, Energy Convers. Manag. 2002; 43:1323-1337.

[41] Bergman T.L., Lavine A.S., Incropeara F.P., Dewitt D.P. Fundamentals of Heat and Mass Transfer. Seventh Edition. John Wiley & Sons, Inc 2011.

[42] L. Nielsen and R. Leithner, "Modelling and Dynamic Simulation of an Underground Cavern for Operation in an Innovative Compressed Air Energy Storage Plant," Energy, Environment, Ecosystem, Development and Landscape Architecture, pp. 285-293, 2009.

[43] Mandhapati Raju, Siddhartha Kumar Khaitan. Modeling and simulation of compressed air storage in caverns: A case study of the Huntorf plant. Applied Energy 2012; 89:474–481

[44] VDI-Gesellschaft Verfahrenstechnik und Chemieingenieurwesen. VDI Heat Atlas, Springer-Verlag Berlin Heidelberg 2010.

[45] Nithyanandam, R. Pitchumani. Cost and performance analysis of concentrating solar power systems with integrated latent thermal energy storage. Energy 2014; 64:793-810

[46] R. Kushnir, A. Dayan, A. Ullmann. Temperature and pressure variations within compressed air energy storage caverns. International Journal of Heat and Mass Transfer 2012; 55:5616–5630.

[47] Kelley, K., 1960. Contribution to the data on theoretical metallurgy: XIII high-temperature heat-content, heat-capacity, and entropy data for the elements and inorganic compounds, U.S. Bur. Mines Bull. No. 584, U.S. Government Printing Office.